RESEARCH ARTICLE

Non-trivial topological spin-polarized surface states induced nonreciprocal transport in the hourglass semimetal

Zahir Muhammad[a], Ghulam Hussain[b,c], Zia ur Rehaman[d], Rajibul Islam[a,*], Igor Antoniazzi[e], Muhammad Ismail Khan[a], Carmine Autieri[f], Maciej R. Molas[e], Xiaoguang Li[b,c], Xiaoyang Lin[a,*], Azizur Rahman[a,*], Weisheng Zhao[a]

[a]National Key Laboratory of Spintronics, Hangzhou International Innovation Institute, Beihang University, Hangzhou 311115, China
[b]Institute for Advanced Study, Shenzhen University, Shenzhen 518060, China
[c]Institute of Microscale Optoelectronics, Shenzhen University, Shenzhen 518060, China
[d]Nanoscale Synthesis & Research Laboratory, Department of Applied Physics, University of Karachi, Karachi, Pakistan
[e]Faculty of Physics, University of Warsaw, 02-093 Warsaw, Poland
[f]International Research Centre MagTop, Institute of Physics, Polish Academy of Sciences, Aleja Lotników 32/46, PL-02668, Warsaw, Poland
Corresponding authors. E-mail: rajibul.physics@gmail.com, xylin@buaa.edu.cn, azizur@buaa.edu.cn
Received May 16, 2026; accepted September 4, 2026

Supporting Information

S1. Experiments and Methods

Bulk crystal synthesis:

Bulk crystal synthesis: Ta_3GeTe_6 single crystals were synthesized by using CVT. The precursor materials of Ta, Ge and Te, with a 3: 2: 6 stoichiometric ratio (total mass of 2 mg), were mixed and ground together to form a homogeneous mixture, with a slight excess of Te (less than 5 wt.%) added to compensate for its volatility during the high-temperature growth process. Then the mixture was transferred to a silica ampoule with an inner diameter of 10 mm, a wall thickness of 2 mm, and a length of 20 cm (internal volume $\approx 15.71\ cm^3$). Resublimed iodine (I_2) with a mass of 35 mg ($\sim 2.23\ mg/cm^3$) was added to act as the transport agent. The ampoule was evacuated and sealed under a vacuum pressure of 10^{-4} Torr. Thereafter, the ampoule was loaded coaxially into a two-zone furnace, and the temperature of the furnace was raised with a gradient of $1\ ^\circ C/minute$ until both its zones reached 750 $^\circ C$. It was kept at this temperature for 6 days and was subsequently reduced to get a high-temperature zone at 600 ^oC, while the low-temperature zone was maintained at 550 ^oC. The furnace was allowed to operate at this temperature for the next 7 days before naturally cooling to room temperature. This experiment yielded high-quality single crystals of Ta_3GeTe_6, which were utilized for further investigation thereafter.

ARPES Measurement:

Angle-resolved photoemission spectroscopy (ARPES) measurements on Ta_3GeTe_2 were performed at the BL13U beamline of the National Synchrotron Radiation Laboratory (NSRL) in Hefei. Using a Scienta DA30L electron spectrometer and horizontally polarized light with photon energies from 20 to 33 eV, the electronic structure was mapped. The sample was cleaved in situ at 12 K and measured at 8 K in an ultrahigh vacuum better than 1.6×10^{-11} mbar. The energy and angular resolutions were 15 meV and 0.2°, respectively.

Device fabrication and transport measurements:

The High-quality Ta_3GeTe_6 flakes were mechanically exfoliated from bulk crystals using white Scotch Magic tape. The exfoliated layers were first transferred onto a flexible polydimethylsiloxane (PDMS) substrate, and the uniform contrast and suitable thickness were identified under an optical microscope. The selected layers were sequentially transferred onto a pre-patterned Hall bar with a width of 5 μm (prepared by standard photolithography technique and Ar ion milling with a Ti(10 nm)/Au(50 nm) electrodes). The device was wire-bonded to a rotatable sample holder using aluminum wires and loaded into a Physical Property Measurement System (PPMS, Quantum Design) for transport measurements. A sinusoidal AC current at 13 Hz was supplied by a Keithley 6221 current source. The resulting first-harmonic and second-harmonic voltage signals were measured using two Stanford Research SR830 lock-in amplifiers, configured to detect the in-phase (0°) and out-of-phase (90°) components, respectively. By shifting the phase reference of the lock-in amplifier by 180°, we successfully isolated the phase-resolved directional transport characteristics corresponding to the effective forward ($I_{ac} > 0$) and backward ($I_{ac} < 0$) current directions, as shown in Fig. 2(e).

Raman Measurements:

Polarization-resolved Raman scattering measurements were conducted at ambient temperature using a 515 nm diode laser with a power of 2 mW. Reflected laser light and Rayleigh scattering were suppressed using a 515 nm Bragg-grating notch filter. For the angle-dependent measurements, a λ/2 plate was placed after the objective to simultaneously rotate the polarization of both the incident and scattered light with respect to the crystal axes, while maintaining propagation along the sample's z-axis. Raman spectra were collected in both co-polarized (XX) and cross-polarized (XY) configurations.

Density functional theory calculations:

Density functional theory (DFT) calculations were carried out using the VASP package [1]. The core and valence electrons are considered within the projector augmented wave method by taking a cutoff of 600 eV for the plane wave basis [2, 3]. For structural optimization, both the volume and atomic position relaxations are performed until the force and energy differences were less than 0.001 eV/Å and 10^{-8} eV, respectively. An appropriate *k*-mesh $8 \times 6 \times 4$ was chosen for each structure depending on the lattice parameters. All the electronic band structure calculations were performed by considering the spin-orbit coupling (SOC) effects. The calculations for the surface states were performed using the semi-

infinite Green's function approach integrated in the WannierTools [4, 5].

S2. Supporting results

S2.1. Characterizations

Figure S1 shows the characterization results of Ta_3GeTe_6 single crystals. Figure S1(a) illustrates the single-crystal X-ray diffraction (XRD) of the prepared single crystals. XRD exhibits sharp diffraction peaks, indicating the high quality of the crystalline nature of the grown single crystals, with no impurity peaks, suggesting that the crystals were grown in the pure phase. The crystals have grown along the (0X0) direction, with a preferred growth orientation along the (080) direction. Figure S1(b) shows the integrated core-level photoemission spectrum of the cleaved surface of the Ta_3GeTe_6 single crystal. It is seen that the spectrum displays Ta 4f, Ge 3d and Te 4d spin-orbit splitting doublets, which can confirm the chemical structure of the Ta_3GeTe_6 crystal. The Ta 4f states lie within 22 and 26 eV, originating from the Ta surface's chemical shift, and Ge 3d states occupy around 30 eV. The peak within 39 to 42 eV is allocated to the Te 4d orbitals, attributed to the Te surface. The energy-dispersive X-ray spectroscopy (EDS) and elemental mapping were performed on the single crystal (see SEM image in Figure S1(a)) with corresponding EDS spectra (see Figure S1(b)) and their mapping elucidating that all three elements (Ta, Ge, and Te) are uniformly distributed throughout the crystals without any aggregation (see Figure S1(c)). The EDS spectra taken from the Ta_3GeTe_6 surface in Figure S1(b) depict the stoichiometric ratio of the constituent elements i.e., Ta, Ge, and Te, respectively, which are nearly 3:1:6.

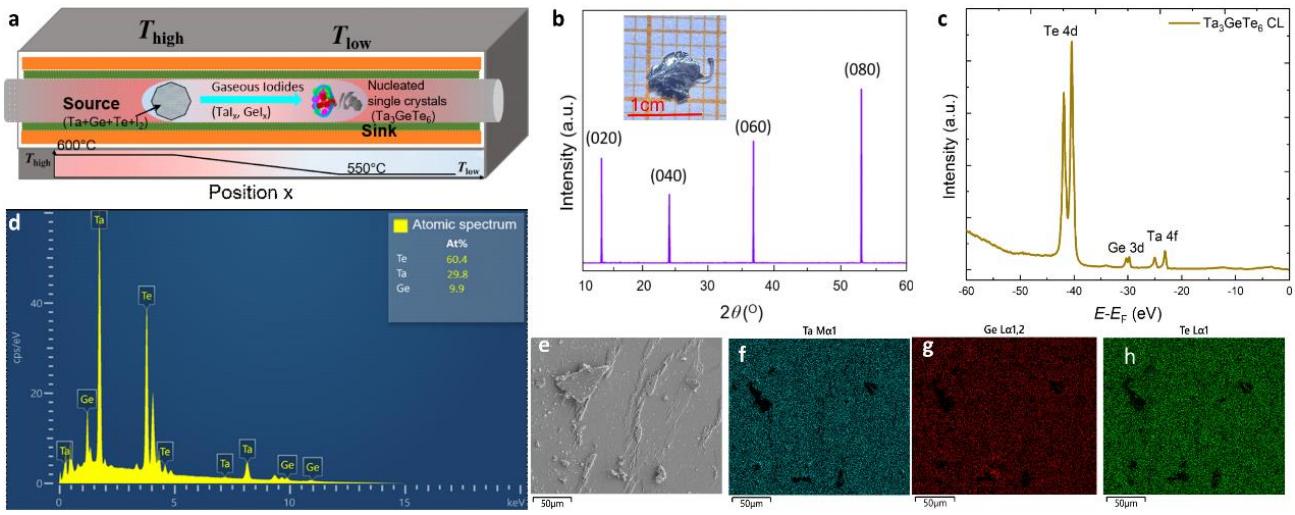

Figure S1 Synthesis and characterization of Ta_3GeTe_6 bulk crystal. (a) schematic of the CVT furnace used to grow the Ta_3GeTe_6 bulk crystal growth via iodine vapor transport. (b) Single-crystal X-ray diffraction (XRD) pattern of the as-grown Ta_3GeTe_6 crystal, showing sharp peaks corresponding to the (0*l*0) family of planes. The inset shows an optical photograph of a typical as-grown single crystal placed on a millimeter-grid background (scale bar is 1 cm), showcasing its characteristic morphology and metallic luster. (c) Core level spectra of the Ta_3GeTe_6, showing the Ta, Ge and Te peaks. (d) EDS spectrum of Ta_3GeTe_6, with the inset table showing the obtained composition from the spectrum data of the region from the SEM image (e) and their corresponding Mapping images show Ta, Ge and Te, respectively.

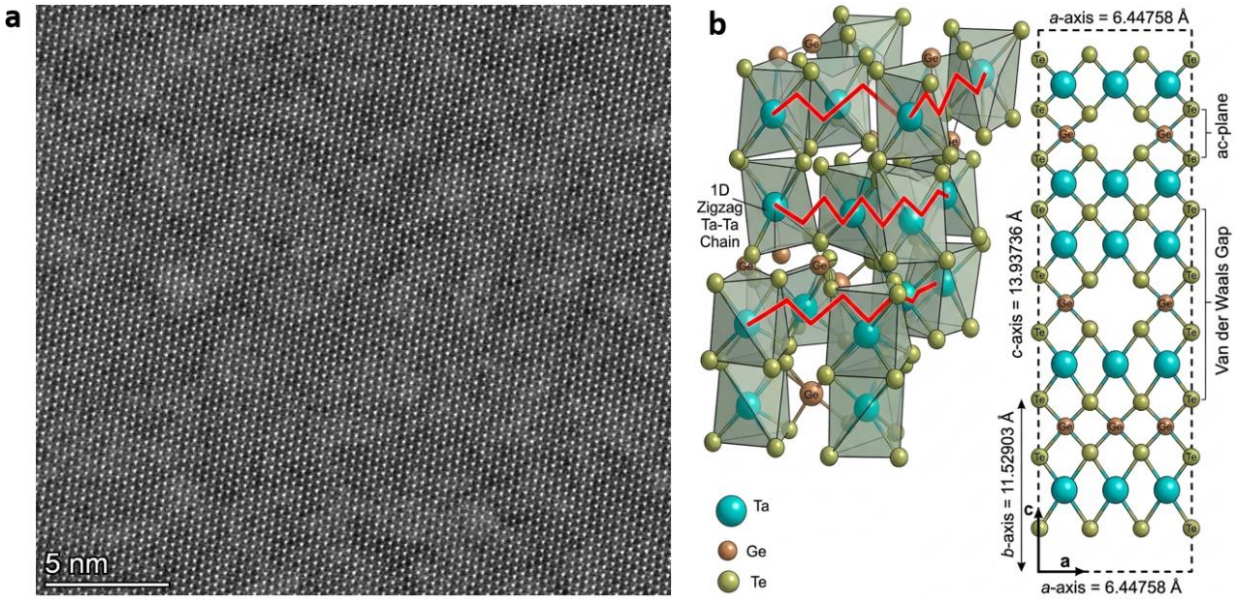

Figure S2 (a) Microstructure of the Ta_3GeTe_6 using STEM measurement and (b) crystal structure representation using base vectors and vdW bonding, making the zigzag chain.

S2.2. ARPES Measurement

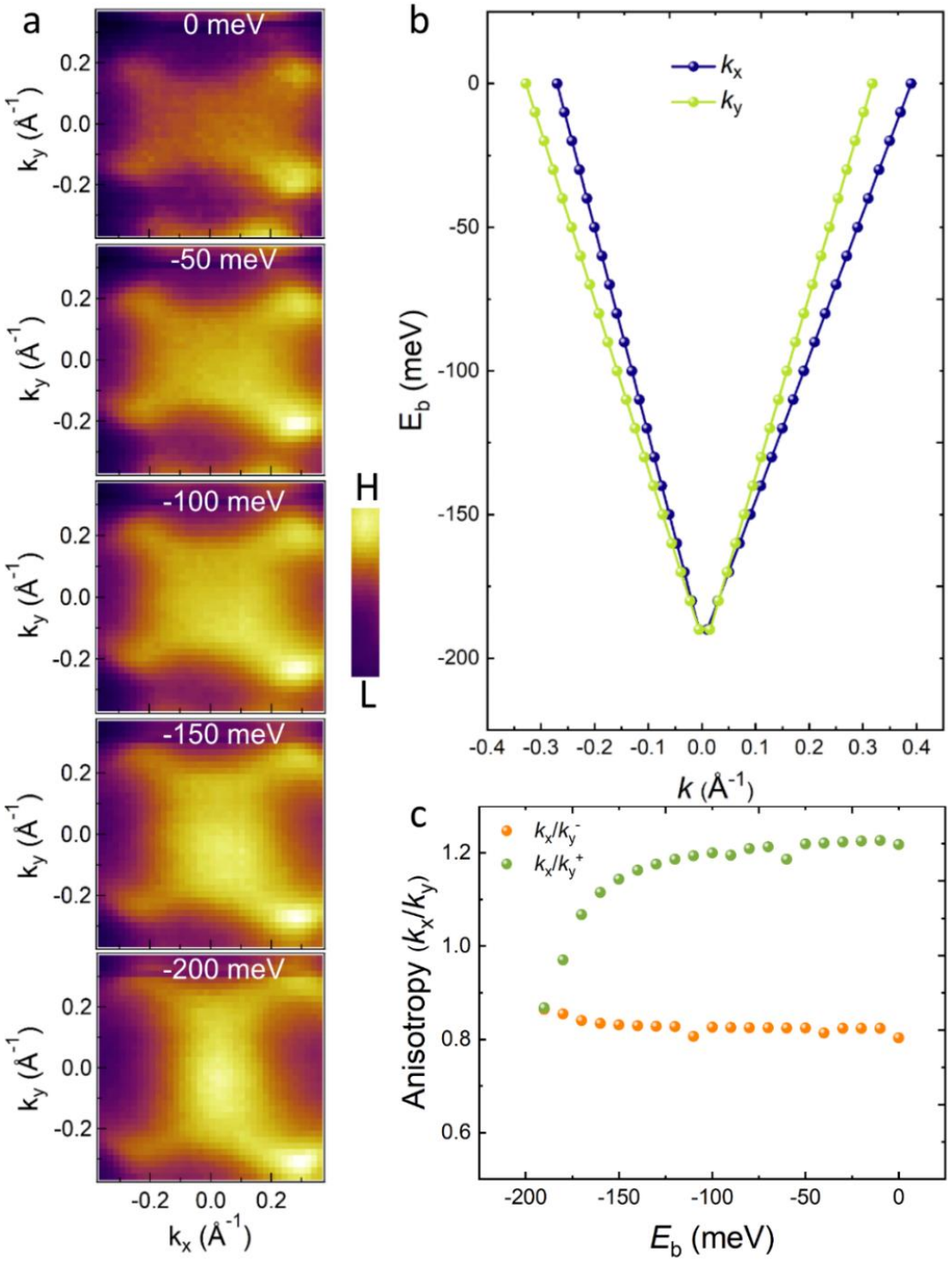

Figure S3 (a) CEC plots at different binding energies, (b) k_x and k_y representation as a function of different binding energies and (c) shows the calculated anisotropy representation of the FS at different binding energies.

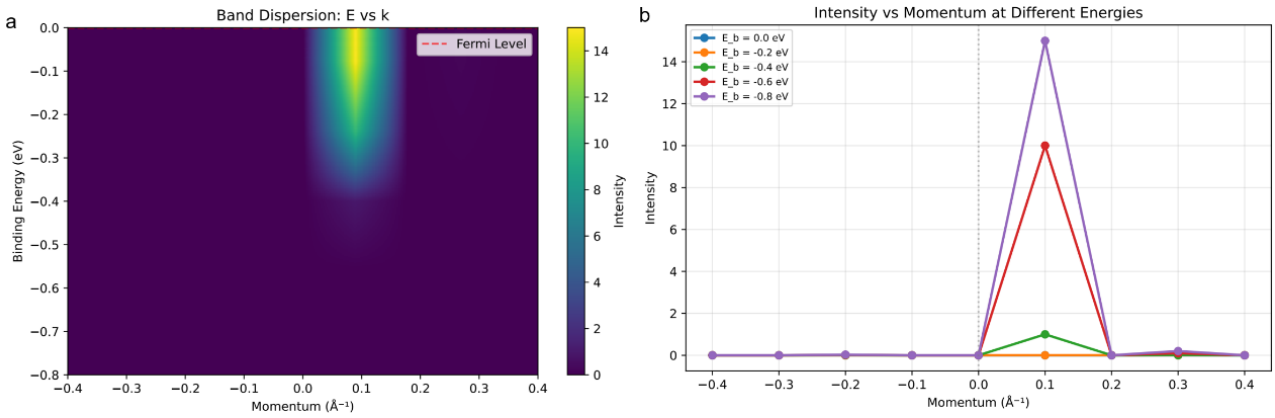

Figure S4 Nodal line analysis. (a) Figure S5: Single line shows the Nodal line dispersion along *k*-space and (b) variation of intensity as a function of binding energies, respectively.

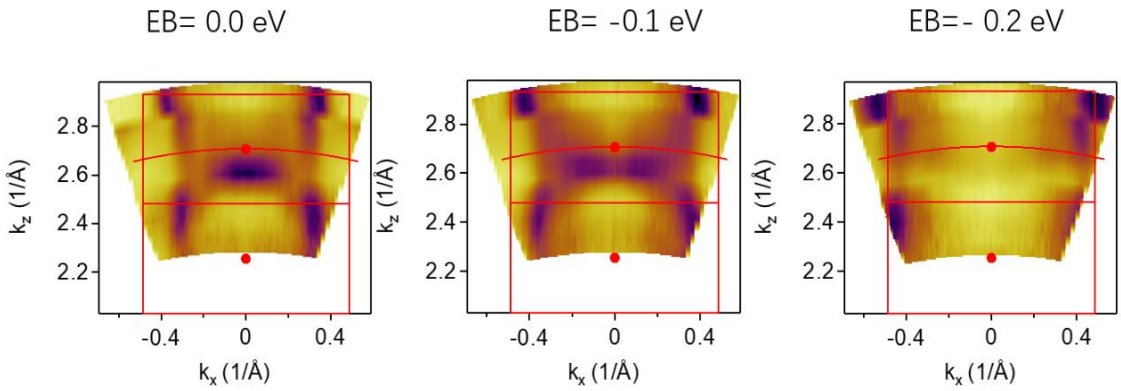

Figure S5 Photon energy dependence contour plots along k_x and k_z of Ta_3GeTe_6. The measurements was taken from 20 eV to 33 eV.

S2.3. Transport Results:

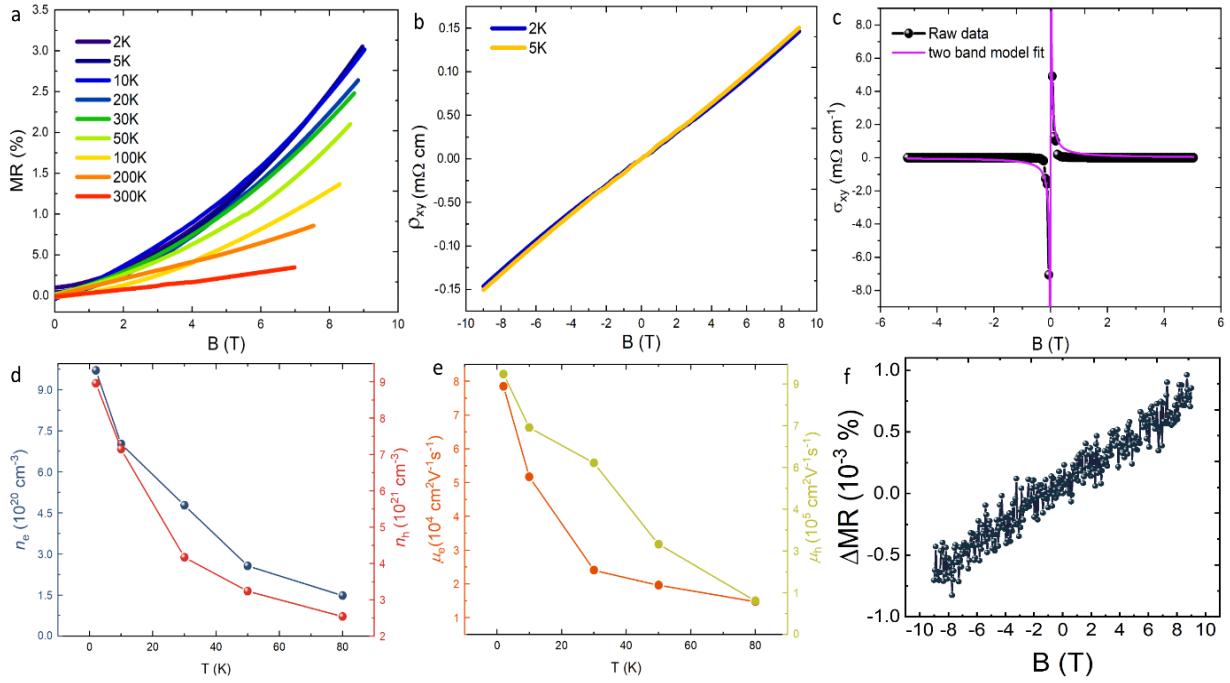

Figure S6 Transport measurements and analysis. (a) MR at different temperatures, (b) transverse resistivity (ρ_{xy}) at 2 K and 5 K, and (c) two-band model fitting for 2 K. (d & e) carrier concentration and mobility of electrons and holes as a function of temperature, respectively. (f) The magnitude of nonreciprocal MR linearly increases with increasing applied *B*.

S2.4. Polarized Raman spectroscopy

The phonon dispersion of the bulk Ta_3GeTe_6 sample was studied using angle-resolved polarized Raman scattering (ARPRS) to demonstrate the anisotropic features of phonon dispersion related to the crystal orientation. It is indicated that the Ta_3GeTe_6 shows a very rich Raman spectrum of 21 modes from the 70 to 180 cm^{-1} range. The ARPRS was measured under two different polarization configurations to explore the phonon anisotropy in our grown crystal. Figure S6(b) and (c) represent the contour plots of ARPRS for co-(XX)-and cross-(XY)-polarization configurations. It is affirmed from both polarization configurations that the RS shows different intensities at varying angles. At XX configuration, each mode of RS below 130 cm^{-1} shows two-fold symmetry except the modes at 87 and 103 cm^{-1}, while, for XY configuration the RS illustrates four-fold symmetry for all modes apart from the mode at 92 cm^{-1}. At the same time, the Raman mode 180 cm^{-1} is not observed in the XY configuration, indicating an out-of-plane symmetry of this mode. Furthermore, we have analyzed the Raman modes above 130 cm^{-1} due to unclear intensities of these modes for both polarization by using polar plots of the integrated intensities, as shown in Figures S6(d-i). Figure S6(d-i) represents the polar plots of Raman intensity and fitted curves (grey dashed line) of the observed six Raman-active modes above 130 cm^{-1} for both co-and cross-polarization, respectively. The dashed curves in Figures S6(d-i) depict the fits of the

mode intensities as a function of light polarization, $I(\theta)$, by the relation [6]:

$$I(\theta) = (|A|\sin^2(\theta - \phi) + |C|\cos(\alpha)\cos^2(\theta - \phi))^2 + |C|^2\sin^2(\alpha)\cos^4(\theta - \phi) \quad (1)$$

where |A| and |C| indicate the amplitudes of the phonon modes, ϕ denotes the phase of polarization dependence, and α is the phase difference. The results indicate that the four modes under XX-polarization show 2-fold symmetry (see Figures 4(d-g)), and two modes (163 and 166 cm^{-1}, see Figure S6(h & i)) illustrate 4-fold symmetry. Whereas, for XY-polarization configuration, all the Raman modes above 130 cm^{-1} show 4-fold symmetry except the mode at 149 cm^{-1} (see Figure S6(f)) doesn't show any polarization dependence. The Raman results demonstrate that the phonons are anisotropic for both XX and XY polarization configurations, which is associated with the crystal symmetry of Ta_3GeTe_2. Our results demonstrate that not only the electronic but also the phononic properties of this van der Wall system are anisotropic, which can be associated with our crystal structure, which can show the unidirectional magnetoresistance.

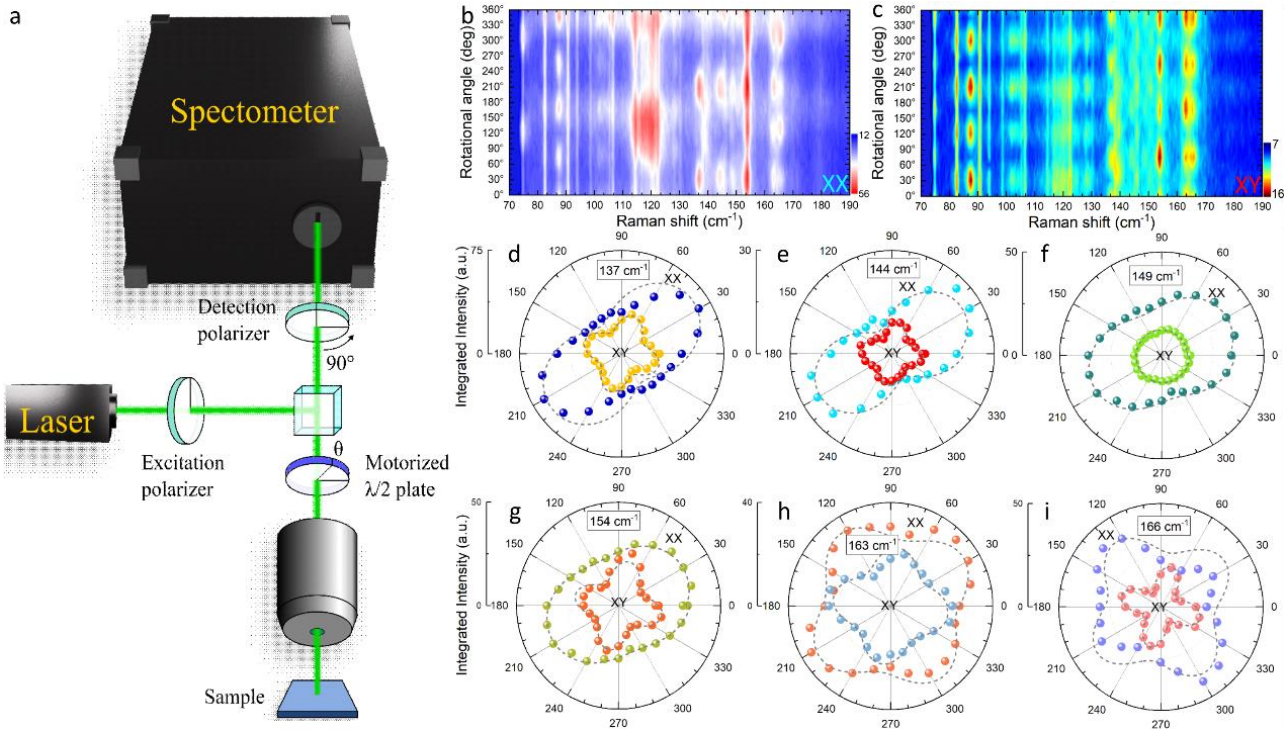

Figure S7 RS of the Bulk Ta_3GeTe_6. (a) Schematic illustration of the Raman measurement (b, c) contour plots of the ARPRS and (d-i) polarization dependence of the integrated intensity of the Raman modes (137, 144, 149, 154, 163 and 166 cm^{-1}) for co-and cross-polarization configurations, respectively. The grey dashed line shows the fitting.

References

S1. G. Rikken, P. Wyder, Magnetoelectric anisotropy in diffusive transport, *Phys. Rev. Lett.* **94**, 016601 (2005).

S2. a) G. Kresse, J. Hafner, Ab initio molecular dynamics for liquid metals, *Phys. Rev. B* **47**, 558 (1993);

b) G. Kresse, J. Furthmüller, Efficiency of ab-initio total energy calculations for metals and semiconductors using a plane-wave basis set, *Comput. Mater. Sci*. **6**, 15 (1996).

S3. G. Kresse, D. Joubert, From ultrasoft pseudopotentials to the projector augmented-wave method, *Phys. Rev. B* **59**, 1758 (1999).

S4. Q. Wu, S. Zhang, H.-F. Song, M. Troyer, A. A.Soluyanov, WannierTools: An open-source software package for novel topological materials, *Comput. Phys. Commun*. **224**, 405 (2018).

S5. M. P. L. Sancho, J. M. L. Sancho, J. Rubio, Highly convergent schemes for the calculation of bulk and surface Green functions, *J. Phys. F Metal. Phys.* **15**, 851 (1985).

S6. H. B. Ribeiro, M. A. Pimenta, C. J. D. Matos, R. L. Moreira, A. S. Rodin, J. D. Zapata, E. A. D. Souza, and A. H. C. Neto, Unusual angular dependence of the Raman response in black phosphorus, ACS Nano 9, 4270 (2015).